

MediSyn: Text-Guided Diffusion Models for Broad Medical 2D and 3D Image Synthesis

Cho Joseph^{1*†}, Zakka Cyril^{1†}, Shad Rohan², Wightman Ross³,
Chaudhari Akshay⁴, Hiesinger William^{1*†}

¹Department of Cardiothoracic Surgery, Stanford Medicine.

²Division of Cardiovascular Surgery, Penn Medicine.

³Research Division, HuggingFace.

⁴Radiology & Integrative Biomedical Imaging Informatics, Stanford Medicine.

*Corresponding author(s). E-mail(s): jcho5@stanford.edu;
willhies@stanford.edu;

†These authors contributed equally to this work.

Abstract

Diffusion models have recently gained significant traction due to their ability to generate high-fidelity and diverse images and videos conditioned on text prompts. In medicine, this application promises to address the critical challenge of data scarcity, a consequence of barriers in data sharing, stringent patient privacy regulations, and disparities in patient population and demographics. By generating realistic and varying medical 2D and 3D images, these models offer a rich, privacy-respecting resource for algorithmic training and research. To this end, we introduce MediSyn, a pair of instruction-tuned text-guided latent diffusion models with the ability to generate high-fidelity and diverse medical 2D and 3D images across specialties and modalities. Through established metrics, we show significant improvement in broad medical image and video synthesis guided by text prompts.

1 Introduction

Deep learning in medicine has made remarkable strides, with applications ranging from diagnostic imaging to predictive analytics [1–3]. The fusion of advanced computational

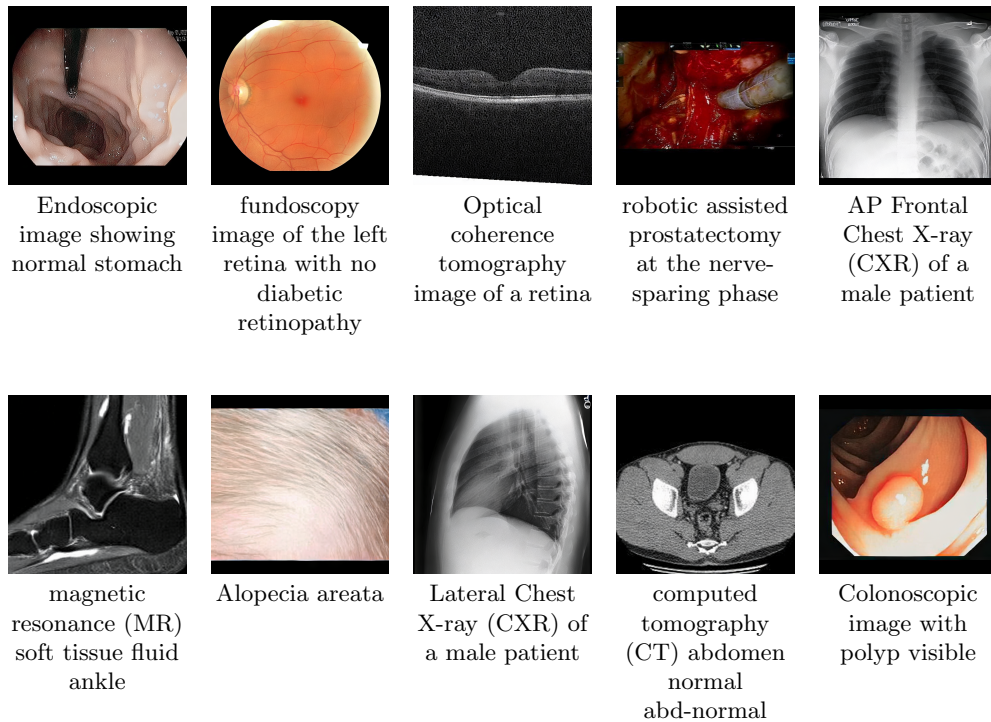


Fig. 1: Series of medical images generated by Medisyn’s 2D model, where the accompanying captions serve as the text prompts for the model

techniques with medical expertise has enabled the development of models that can identify patterns in complex datasets, offering unprecedented insights into patient care and disease management [4–6]. These successes have not only enhanced diagnostic and therapeutic capabilities but have also opened new avenues for personalized medicine, augmenting the potential for tailored patient care.

However, the paucity of high-quality annotated datasets remains a fundamental barrier to the development of machine learning models in the medical field. While large volumes of data are generated by the healthcare industry worldwide, annotating these datasets comes at a significant cost due to the extensive domain expertise and time commitment involved [7, 8]. Additionally, underlying medico-legal constraints surrounding the acquisition and dispersion of medical data pose an import barrier to the aggregation of data at the scale needed for the development of machine learning tasks [9]. To add to this, medical data often reflects the disease distribution of a population, leading to imbalanced datasets with marked disparities in illness incidence and prevalence rates. These obstacles, coupled with the under-representation of certain populations in medical settings, can result in biased and fallible clinical support decision systems that fail to generalize to new settings and population groups [10, 11].

In recent years, denoising diffusion models probabilistic (DDPMs) have garnered immense interest due to their ability to synthesize diverse and high-fidelity images [12,

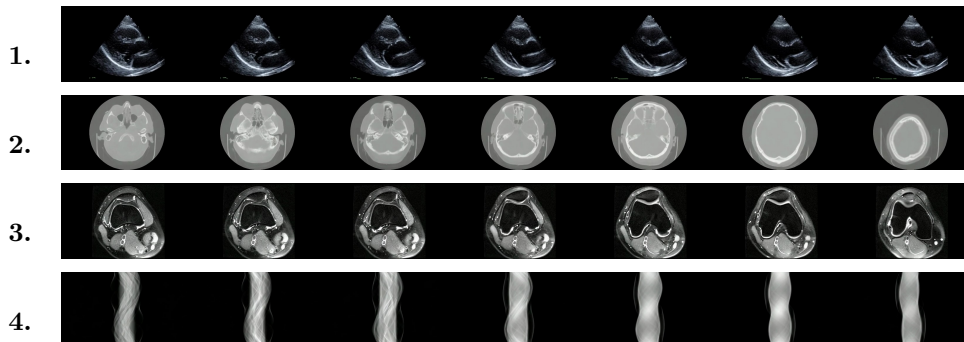


Fig. 2: Outputs generated by Medisyn’s 3D model and their corresponding textual prompts are: (1) “This echocardiogram shows normal left ventricular systolic function and qualitatively normal right ventricular function in a child. No significant heart valve dysfunction, pericardial effusion, nor mitral valve regurgitation are present.”, (2) “normal head CT”, (3) “knee MRI in the axial plane”, and (4) “high-quality simulated abnormal head CT sinogram”. Please note these outputs are subsets of our full videos (32 frames).

13]. By decomposing the generation task into a sequence of denoising steps, diffusion models have achieved state-of-the-art results on perceived output quality and data distribution metrics. Additionally, advancements in text embeddings [14, 15] have enabled DDPMs to incorporate textual prompts, allowing for precise control over the image generation process. Derived from DDPMs, latent diffusion models (LDMs) are increasingly used due to their efficient denoising operations in latent space [16–18]. Such models have also been utilized to generate videos by incorporating temporal functionalities [19, 20].

In this work, we focus on the ability of LDMs to generate novel datasets to overcome class imbalances traditionally associated with medical data, and potentially reduce the need for manual annotation of medical 2D and 3D data. We present MediSyn, a pair of text-guided latent diffusion models for broad medical 2D and 3D modality synthesis. To overcome the scarcity of labelled medical data, we leverage a vast corpus of more than 5 million image-caption pairs and 100,000 video-caption pairs collected from the public domain across numerous medical specialties, and integrate comprehensive natural language annotations to develop a pair of versatile diffusion models for the medical domain.

2 Related Work

Since their introduction, generative models have had a rich history in the medical field, ranging from anomaly detection and image denoising [21, 22], to image reconstruction and segmentation [23, 24]. For instance, DDPMs have been trained to convert MRIs to CTs for soft tissue injury [25], synthesize labeled brain MRIs for training segmentation

models [26], denoise OCTs to erase visual artifacts [27], and reconstruct images for accelerated MRI scans [28].

Our work, akin to Sagers et al. and Chambon et al. focuses on synthesizing multi-class medical datasets through text prompts. In their work, Chambon et al. adapt a pre-trained LDM, Stable Diffusion, on a corpus of chest x-rays (CXR) and their corresponding radiology reports to generate CXR displaying different disease states [29]. Similarly, Sagers et al. use DALL-E to synthesize skin lesions across all Fitzpatrick skin types [30].

Despite impressive results, the lack of large, curated, publicly available medical imaging datasets makes training these models challenging, often resulting in outputs with limited diversity and realism [31]. The resulting outputs, despite being visually impressive, are often constrained to a single imaging modality type or medical subspecialty which restricts their utility outside the scope of their defined tasks. While adopting a similar approach to the works outlined above, our research stands out in several ways:

- We collect and train on one of the largest publicly available datasets of medical images and videos to date, spanning more than 5 million image-caption pairs and 100,000 video-caption pairs (comprised of volumetric scans and image sequences) across 8 broad specialties and 9 image types.
- We present a method to generate high-fidelity, high-resolution, and diverse medical images from a fine-tuned 2D LDM
- Similarly, we demonstrate the ability to synthesize high-quality, coherent, and varying medical image sequences and volumetric scans in video format from a fine-tuned 3D LDM
- We demonstrate significant improvements in the generated outputs through standard metrics.

3 Methods

3.1 Description of the Dataset

We assembled a set of 5,785,333 medical image-caption pairs, covering 8 specialties and 9 imaging modalities, to train Medisyn’s 2D model. We reserved an additional 1000 image-caption pairs (125 pairs from each specialty) for model evaluation.

For Medisyn 3D, we compiled a total of 107,216 medical video-caption pairs, spanning 2 specialties and 3 imaging modalities. We performed model evaluation on a separate set of 200 pairs (100 from each specialty). Summary statistics for the entire dataset is provided in Table 1.

3.1.1 Structured Public Dataset Collection

A collection of publicly available medical datasets spanning several machine learning tasks (e.g. classification, regression) is aggregated and processed. Each dataset is manually converted into an *image-text* or *video-text* format as appropriate by combining all available metadata and labels into a single caption. The resulting dataset is spot checked to ensure high quality dataset generation.

3.1.2 Unstructured Public Dataset Collection

Similarly, there exists a variety of reference medical websites showcasing disease states, case reports, and collections. We construct website-specific pipelines to download and process all modality-caption pairs encountered and append them to our dataset, while adhering to polite scraping strategies and responsible data usage. All data is spot checked for modality and caption quality.

Specialty	Number of Pairs	Modality Type	Number of Pairs
		X-rays (XR)	856,682
Radiology	3,106,264	Computerized Tomography (CT)	1,150,206
Dermatology	79,209	Magnetic Resonance Imaging (MRI)	699,105
Cardiology	177,275	Ultrasound (US)	435,900
Gastroenterology	7,568	Electrocardiogram (ECG)	141,566
Pathology	197,310	Microscopy Images	197,310
General Surgery	2,150,757	Light Photography	174,246
Ophthalmology	174,246	Spectrograms	920
Pulmonology	920	Surgical Footage	2,150,757

(a) Dataset Breakdown per Specialty

(b) Dataset Breakdown per Modality

Table 1: Dataset breakdown summary

3.2 Data Pre-processing

We apply the same sequence of processing steps to our collected images. First, we resize the longer dimension of each image to 1,152 pixels while proportionally scaling the shorter edge to maintain the original aspect ratio. Next, we pad the shorter edge with black pixels, thus obtaining a square image of 1,152x1,152 pixels. Last, we perform a center crop on every image for a resulting size of 1,024x1,024 pixels.

For Medisyn’s 3D model, we randomly selected 32 consecutive images or slices from each video and appended black frames to those short of 32 frames. Next, we resize each frame to a height of 256 pixels, while scaling the width to maintain aspect ratio. Last, we either perform cropping or padding with black pixels to achieve a width of 448 pixels.

3.3 Image Generation

Despite the prevalent use of Stable Diffusion for medical text-to-image tasks [29, 32, 33], we sought for a more computationally fast architecture. We thus adopted Würstchen v2, a text-to-image LDM with a 42x spatial compression rate [34]. This image compression leads to an eightfold reduction in GPU training time relative to

Stable Diffusion 2.1, while maintaining comparable image fidelity. Würstchen’s model architecture is structured as a three-stage pipeline. Stages A and B encode the images into highly compressed latent representations, while Stage C synthesizes (denoises) them with text-conditioning. All textual prompts were embedded using a frozen CLIP text encoder.

To prevent unnecessary training, we conducted ablative experiments to assess which stages of Würstchen required fine-tuning on our medical dataset. Details of these studies, along with their architectures, are found in the Appendix 6.3. Our findings revealed that both Stages A and B were effective in compressing and upsampling images from our medical dataset. In contrast, Stage C failed to synthesize latent samples that align with real medical images, so we proceeded with fine tuning its text-conditional LDM on our medical *image-text* pairs.

For fine-tuning the pretrained LDM, we closely followed the original training specifications (learning rate, optimizer, loss function, etc.) with a few adjustments. We trained the model for roughly three epochs of the training set with a learning rate of $1e-4$ and an effective batch size of 256. We initiated an exponential moving average (EMA) of the model’s parameters at 1500 steps and subsequently updated it every 100 steps. Text captions were dropped 5 percent of the time to enable Classifier-Free Guidance (CFG) [35]. This method allows us to trade off between image diversity and fidelity by controlling the CFG scale (a parameter). Higher values help increase alignment to textual prompts, while lower values lead to stronger mode coverage. We conducted training on 4 A100 GPUs using PyTorch’s Distributed Data Parallel (DDP) [36], spanning roughly 4 days.

3.4 Video Generation

Video synthesis is notably more difficult than image synthesis primarily due to the need for both spatial and temporal coherence [37]. To help overcome this, we proceed with HiGen, a text-to-video LDM that decouples spatial and temporal processing across two distinct stages: structure and content [38]. HiGen incorporates a Variational Autoencoder (VAE) for encoding and decoding frames, a 3D U-Net for noise estimation (synthesis), and a frozen CLIP encoder for embedding textual prompts. In the structure phase, the U-Net incorporates the middle frames of the videos as spatial priors, alongside the corresponding embedded texts. To further increase temporal consistency, the content level introduces embeddings of motion and appearance variations from the corresponding videos. Motion vectors are derived from pixel-wise differences between consecutive frames, while appearance values are obtained from the image encoder of DINOv2 [39].

Similarly to Würstchen, we examined which components of HiGen required fine-tuning on our medical dataset, with the exception of the CLIP text encoder which remained frozen (Appendix 6.3). Although the VAE was performant in encoding and decompressing our medical videos, the 3D U-Net failed to synthesize samples that resemble real medical data. Thus, we proceeded with fine-tuning the U-Net on our medical *video-text* pairs.

We loosely follow the original training method, incorporating several modifications. With equivalent compute (8 A100 80GB GPUs), we allocate half of the GPUs for

video training and the other half for images: both spatial and temporal layers of the U-Net are not aligned to medical data. Prior to training, we preprocess the videos and compute their appearance changes using the ViT-B/8 version of DINOv2. For image training, we use the middle frames of the medical videos as the model inputs. We trained for a total of 10053 steps with a learning rate of 5e-5, covering roughly 3 epochs of the video dataset. We set the effective batch size for videos and images to 32 and 512, respectively. We dropped text captions 10% of the time. The entire training process was completed in roughly 12 hours.

3.5 Evaluation

Due to the lack of text-to-image models trained on broad medical data, we opted to use the pretrained Würstchen v2 as our baseline model. For each textual prompt from our test set, we generated corresponding images using Würstchen v2 and our fine-tuned version at all three checkpoints. We set the CFG scale to 6.0 across all models, and fixed the image generation size at 1024x1024 pixels. For our metric, we chose Fréchet Inception Distance (FID) [40], which measures the fidelity and diversity of the set of generated images relative to the original ones. For HiGen, we similarly benchmark our fine-tuned versions against the pretrained model. We set the CFG scale to 12.0 for all models, and fixed the dimensions of the generated videos to 448 pixels in width and 256 pixels in height. The video frame length was set to 32. We set the appearance factor to 0.7 and motion factor to 300. We used the Fréchet Video Distance (FVD) [41] as our quantitative metric. FVD builds on FID by incorporating temporal information: embeddings are computed using Inflated 3D ConvNet, a video classification model.

$$FID(x, y) = \|\mu_x - \mu_y\|^2 + Tr(\Sigma_x + \Sigma_y - 2(\Sigma_x \Sigma_y)^{1/2})$$

Fig. 3: In the FID formula, x and y represent the feature vectors of the generated and original images respectively (extracted via Inception v3 model), μ_x and μ_y denote their mean vectors respectively, Σ_x and Σ_y refer to their covariance matrices respectively, and Tr is the trace of a matrix (sum of its diagonal entries). Low FID values indicate similar distributions whereas high values suggest dissimilar ones.

4 Results

For both the 2D and 3D models, we observed that all of our fine-tuned versions significantly outperformed their pretrained counterparts. We noticed the FID of our 2D model, both with and without EMA, showed substantial decreases of 55.6% and 54.4% respectively by the end of the first epoch, far exceeding the performance of base Würstchen. However, there was no further improvement after epoch 1, suggesting fast overfitting of the medical images. Additionally, performance between the EMA and

Model	FID (Non-EMA)	FID (EMA)	FVD
Pretrained Würstchen v2	-	167.6916	-
Medisyn 2D, end of epoch 1	76.4656	74.4487	-
Medisyn 2D, end of epoch 2	76.3751	74.6191	-
Medisyn 2D, end of epoch 3	84.1539	77.1361	-
Pretrained HiGen	-	-	5046.6630
Medisyn 3D, 3351 steps	-	-	645.7636
Medisyn 3D, 6702 steps	-	-	573.5518
Medisyn 3D, 10053 steps	-	-	472.9926

Table 2: Evaluation results for Medisyn and its pretrained counterparts. Lower FID/FVD values indicate superior performance (more similar to distribution of original medical images/videos).

non-EMA versions was nearly identical (differing by no more than 8.7%), suggesting that incorporating EMA may not be necessary.

For our 3D model, we observe that the FVD notably decreased by 87.2% by the end of epoch 1, far surpassing the pretrained version. Unlike Würstchen, HiGen displayed consistent improvement after the first epoch (an average decrease of 14.4%), implying a capacity for further training.

5 Discussion

Our findings demonstrate Medisyn’s remarkable ability to generate high-fidelity and diverse medical images, image sequences and volumetric scans across various medical subspecialties and imaging modalities. Other medical text-driven diffusion models, such as TauPETGen [42] for tau PET images and GenerateCT [43] for chest CT volumes, have proven successful in generating high-quality images that accurately depict anatomical features and clinical conditions. However, these models are constrained to a single imaging modality and anatomical region, thereby restricting their applicability. Moreover, they were trained on relatively small datasets sourced from a limited number of institutions, which could lead to more biased outputs. In contrast, Medisyn, having been trained on one of the largest publicly accessible medical image and video datasets to date, is equipped to synthesize data that cover numerous medical disciplines, population groups, and disease states. Leveraging our two models, we can synthesize new medical datasets as well as augment existing ones, potentially improving a wide array of medical machine learning tools, both general and specialized. Additionally, our models can minimize the need to repeatedly fine-tune on specific datasets for generating different imaging modalities, thus reducing computational costs for academic labs.

Our study had several limitations. First, we solely relied on standard quantitative metrics, which fail to measure the clinical relevance of the generated data, specifically their anatomical and pathological accuracy. To address this, we suggest a qualitative evaluation by a team of clinical experts. Second, both our 2D and 3D models face challenges in generating high-fidelity images for certain medical subspecialties and imaging modalities, such as electrocardiograms and brain MRIs, respectively. Third, our 3D model was limited to generating a fixed number of frames—32 for optimal quality. This poses a challenge within medical contexts, where the number of slices or

images in medical scans can widely vary. Fourth, we employed frozen, general domain text encoders, which may not fully capture the subtleties present in medical text. We suggest adapting encoders pretrained specifically on medical corpora to further improve results.

Future research should focus on finding ways image and video generative models can more accurately capture and exhibit the anatomical and pathological details of the medical data they’re trained on. This could be achieved through augmenting existing model architectures, using specialized loss functions, among other approaches.

In summary, we introduced a pair of text-conditional LDMs trained on an extensive medical image and video dataset covering various medical subspecialties and imaging modalities. By generating high-fidelity and diverse medical 2D and 3D images, Medisyn illustrates the potential for a singular framework to broadly address the challenge of data scarcity in healthcare.

6 Acknowledgments

We would like to thank Stanford Sherlock for their continuous support with GPU access. We would also like to thank John Ng, Rajiv Gandhi, and the rest of the Oracle team for their generous support with GPU access.

Declarations

6.1 Funding

This project was supported in part by a National Heart, Lung, and Blood Institute (NIH NHLBI) grant (1R01HL157235-01A1) (W.H.).

6.2 Competing interests

The authors declare no competing interests.

6.3 Authors’ contributions

J.C., C.Z. and W.H. designed the experiments. J.C and C.Z. wrote the manuscript. The code-base was authored by J.C and C.Z. Computational experiments were performed by J.C and C.Z.

Appendix

A Würstchen Stages

A.1 Stage A

In Stage A, a Vector Quantized Generative Adversarial Network (VQGAN) encodes a latent representation of the original image. Our objective was to evaluate the performance of the pretrained VQGAN in accurately encoding and reconstructing images from our medical dataset. To examine the fidelity of the reconstructed images, we

used the structural similarity index measure (SSIM), a metric more closely aligned to the human visual system by considering structural information [44]. We selected a random sample of 1,000 images from our training set, processed each one through the VQGAN, and calculated the SSIM between each pair of original and reconstructed images. We obtained an average SSIM of 0.9842, so we skipped fine-tuning this stage.

$$SSIM(x, y) = \frac{(2\mu_x\mu_y + c_1)(2\sigma_{xy} + c_2)}{(\mu_x^2 + \mu_y^2 + c_1)(\sigma_x^2 + \sigma_y^2 + c_2)}$$

Fig. 4: In the SSIM formula, x and y are the two images being compared, μ_x and μ_y represent their mean brightness, σ_x^2 and σ_y^2 denote their variances, σ_{xy} refers to the covariance between the two images, and c_1 and c_2 are constants used to stabilize the division (preventing division by zero). SSIM values range from -1 to 1, where -1 indicates no similarity between the two images and 1 suggests perfect similarity.

A.2 Stage B

Stage B uses an LDM conditioned on an EfficientNet encoding of the original image and the corresponding text to recreate the VQGAN representation. Since its primary role is to refine Stage C’s latent samples, we continued employing the SSIM to allow direct comparison to the given reference image. We passed the same images used in Stage A to the LDM, and subsequently processed the model’s outputs through the VQGAN-decoder to obtain the final images. We calculated the SSIM statistics between the reconstructed images and the original ones. As the average SSIM was 0.8328, we also skipped fine-tuning this stage.

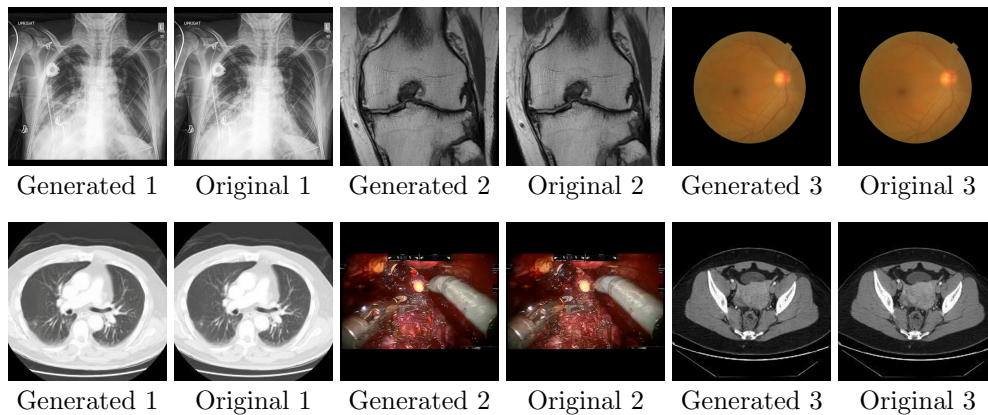


Fig. 5: Würstchen’s two compression stages: comparison of reconstructed images with their original counterparts. The top row shows reconstructions from Stage A, while the bottom row shows images reconstructed starting from Stage B .

A.3 Stage C

Stage C involves training a separate LDM, conditioned on text, in the latent space of the EfficientNet encoder. As this stage is tasked with the actual generation (denoising) of latent samples, we now examine Würstchen as a whole, prompting the model with the same text captions used in the Stage B assessment. Predictably, we observed that none of its generated images bore resemblance to real medical imagery. Thus, we assessed that Stage C, specifically its text-conditional LDM, required fine-tuning on our medical *image-text* pairs.

Model	Average	Median	Standard Deviation	Range
Stage A	0.9842	0.9899	0.0242	0.4545
Stage B	0.8328	0.8649	0.1291	0.9071
VAE	0.9182	0.9502	0.0979	0.3547

Table 3: SSIM statistics across both 2D and 3D LDM components. SSIM values range from -1 to 1, where -1 indicates no similarity between the two images and 1 suggests perfect similarity.

B HiGen components

B.1 VAE

We processed a random set of 50 videos from our training data through the VAE to evaluate its reconstruction abilities. Following the rationale outlined in section A.1, we employed the SSIM on a frame-by-frame basis between the original videos and reconstructed ones. Specifically, we averaged the SSIM values across all frames for each video pair. Noting an average SSIM of 0.9182, we skipped fine-tuning the VAE.

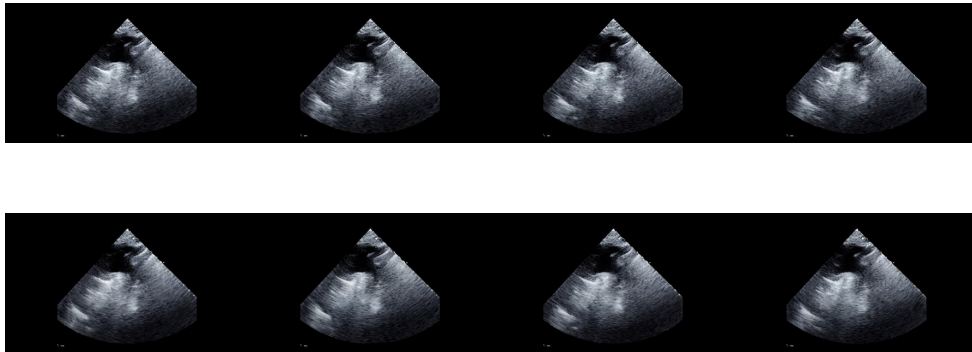


Fig. 6: Comparison of original (top-row) and VAE-reconstructed (bottom-row) images.

B.2 3D U-Net

Akin to Würstchen’s Stage C, this U-Net is responsible for the initial synthesis (denoising) of latents. Consequently, we evaluated the entire HiGen model by using a random set of 200 text captions from our training data for video synthesis, and observed that the generated videos did not resemble their real counterparts. Thus, we proceeded to fine-tune the U-Net on our medical *video-text* pairs.

References

- [1] Tang, Y., Tang, Y., Peng, Y., al.: Automated abnormality classification of chest radiographs using deep convolutional neural networks. *npj Digit. Med.* **3**, 70 (2020)
- [2] Placido, D., Yuan, B., Hjaltelin, J.X., al.: A deep learning algorithm to predict risk of pancreatic cancer from disease trajectories. *Nat Med* **29**, 1113–1122 (2023)
- [3] Dai, L., Sheng, B., Chen, T., al.: A deep learning system for predicting time to progression of diabetic retinopathy. *Nat Med* **30**, 584–594 (2024)
- [4] Amgad, M., Hodge, J.M., Elsebaie, M.A.T., al.: A population-level digital histologic biomarker for enhanced prognosis of invasive breast cancer. *Nat Med* **30**, 85–97 (2024)
- [5] Landi, I., Glicksberg, B.S., Lee, H.C., al.: Deep representation learning of electronic health records to unlock patient stratification at scale. *npj Digit. Med.* **3**, 96 (2020) <https://doi.org/10.1038/s41746-020-0301-z>
- [6] Lu, J., Bender, B., Jin, J.Y., al.: Deep learning prediction of patient response time course from early data via neural-pharmacokinetic/pharmacodynamic modelling. *Nat Mach Intell* **3**, 696–704 (2021)
- [7] Lyu, M., Mei, L., Huang, S., al.: M4raw: A multi-contrast, multi-repetition, multi-channel mri k-space dataset for low-field mri research. *Sci Data* **10**, 264 (2023)
- [8] Liu, C., Leigh, R., Johnson, B., al.: A large public dataset of annotated clinical mris and metadata of patients with acute stroke. *Sci Data* **10**, 548 (2023)
- [9] Kohli, M.D., Summers, R.M., Geis, J.: Medical image data and datasets in the era of machine learning—whitepaper from the 2016 c-mimi meeting dataset session. *J Digit Imaging* **30**, 392–399 (2017) <https://doi.org/10.1007/s10278-017-9976-3>
- [10] Daneshjou, R., Vodrahalli, K., Novoa, R., Jenkins, M., Liang, W., Rotemberg, V., Ko, J., Swetter, S., Bailey, E., Gevaert, O., Mukherjee, P., Phung, M., Yekrang, K., Fong, B., Sahasrabudhe, R., Allerup, J., Okata-Karigane, U., Zou, J., Chiou, A.: Disparities in dermatology ai performance on a diverse, curated clinical image set. *Sci Adv* **8**(32), 6147 (2022)

- [11] Acosta, J.N., Falcone, G.J., Rajpurkar, P., *et al.*: Multimodal biomedical ai. *Nat Med* **28**, 1773–1784 (2022) <https://doi.org/10.1038/s41591-022-01981-2>
- [12] Ho, J., Jain, A., Abbeel, P.: Denoising diffusion probabilistic models (2020) [arXiv:2006.11239](https://arxiv.org/abs/2006.11239) [cs.LG]
- [13] Dhariwal, P., Nichol, A.: Diffusion models beat gans on image synthesis (2021) [arXiv:2105.05233](https://arxiv.org/abs/2105.05233) [cs.LG]
- [14] Radford, A., Kim, J.W., Hallacy, C., Ramesh, A., Goh, G., Agarwal, S., Sastry, G., Askell, A., Mishkin, P., Clark, J., Krueger, G., Sutskever, I.: Learning transferable visual models from natural language supervision (2021) <https://doi.org/10.48550/arXiv.2103.00020> [cs.CV]
- [15] Raffel, C., Shazeer, N., Roberts, A., Lee, K., Narang, S., Matena, M., Zhou, Y., Li, W., Liu, P.J.: Exploring the limits of transfer learning with a unified text-to-text transformer (2019) <https://doi.org/10.48550/arXiv.1910.10683> [cs.LG]
- [16] Rombach, R., Blattmann, A., Lorenz, D., Esser, P., Ommer, B.: High-resolution image synthesis with latent diffusion models (2021) [arXiv:2112.10752](https://arxiv.org/abs/2112.10752) [cs.CV]
- [17] Podell, D., English, Z., Lacey, K., Blattmann, A., Dockhorn, T., Müller, J., Penna, J., Rombach, R.: Sdxl: Improving latent diffusion models for high-resolution image synthesis (2023) [arXiv:2307.01952](https://arxiv.org/abs/2307.01952) [cs.CV]
- [18] Ramesh, A., Dhariwal, P., Nichol, A., Chu, C., Chen, M.: Hierarchical text-conditional image generation with clip latents (2022) [arXiv:2204.06125](https://arxiv.org/abs/2204.06125) [cs.CV]
- [19] Blattmann, A., Rombach, R., Ling, H., Dockhorn, T., Kim, S.W., Fidler, S., Kreis, K.: Align your latents: High-resolution video synthesis with latent diffusion models (2023) [arXiv:2304.08818](https://arxiv.org/abs/2304.08818) [cs.CV]
- [20] Blattmann, A., Dockhorn, T., Kulal, S., Mendelevitch, D., Kilian, M., Lorenz, D., Levi, Y., English, Z., Voleti, V., Letts, A., Jampani, V., Rombach, R.: Stable video diffusion: Scaling latent video diffusion models to large datasets (2023) [arXiv:2311.15127](https://arxiv.org/abs/2311.15127) [cs.CV]
- [21] Schlegl, T., Seeböck, P., Waldstein, S.M., Schmidt-Erfurth, U., Langs, G.: Unsupervised anomaly detection with generative adversarial networks to guide marker discovery **1703** (2017) [arXiv:1703.05921](https://arxiv.org/abs/1703.05921)
- [22] Gondara, L.: Medical image denoising using convolutional denoising autoencoders (2016) [arXiv:1608.04667](https://arxiv.org/abs/1608.04667) [cs.CV]
- [23] Bhadra, S., Zhou, W., Anastasio, M.A.: Medical image reconstruction with image-adaptive priors learned by use of generative adversarial networks (2020) [arXiv:2001.10830](https://arxiv.org/abs/2001.10830) [eess.IV]

- [24] Wu, J., Fu, R., Fang, H., Zhang, Y., Yang, Y., Xiong, H., Liu, H., Xu, Y.: Med-segdiff: Medical image segmentation with diffusion probabilistic model (2022) [arXiv:2211.00611](https://arxiv.org/abs/2211.00611) [cs.CV]
- [25] Lyu, Q., Wang, G.: Conversion between ct and mri images using diffusion and score-matching models (2022) [arXiv:2209.12104](https://arxiv.org/abs/2209.12104) [eess.IV]
- [26] Akbar, U.M., Larsson, M., Blystad, I., al.: Brain tumor segmentation using synthetic mr images - a comparison of gans and diffusion models. *Scientific Data* **11**, 259 (2024) <https://doi.org/10.1038/s41597-024-03073-x>
- [27] Akter, N., Perry, S., Fletcher, J., Simunovic, M., Roy, M.: Automated artifacts and noise removal from optical coherence tomography images using deep learning technique. In: 2020 IEEE Symposium Series on Computational Intelligence (SSCI), pp. 2536–2542 (2020). <https://doi.org/10.1109/SSCI47803.2020.9308336>
- [28] Chung, H., Ye, J.C.: Score-based diffusion models for accelerated mri. *Medical Image Analysis* **80**, 102479 (2022) <https://doi.org/10.1016/j.media.2022.102479>
- [29] Chambon, P., Bluethgen, C., Delbrouck, J.-B., Sluijs, R.V., Polacin, M., Chaves, J.M.Z., Abraham, T.M., Purohit, S., Langlotz, C.P., Chaudhari, A.: Roentgen: Vision-language foundation model for chest x-ray generation (2022) [arXiv:2211.12737](https://arxiv.org/abs/2211.12737) [cs.CV]
- [30] Sagers, L.W., Diao, J.A., Melas-Kyriazi, L., Groh, M., Rajpurkar, P., Adamson, A.S., Rotemberg, V., Daneshjou, R., Manrai, A.K.: Augmenting medical image classifiers with synthetic data from latent diffusion models (2023) [2308.12453](https://arxiv.org/abs/2308.12453) [cs.CV]
- [31] Sagers, L.W., Diao, J.A., Melas-Kyriazi, L., Groh, M., Rajpurkar, P., Adamson, A.S., Rotemberg, V., Daneshjou, R., Manrai, A.K.: Augmenting medical image classifiers with synthetic data from latent diffusion models (2023) [arXiv:2308.12453](https://arxiv.org/abs/2308.12453) [cs.CV]
- [32] Wilde, B., Saha, A., Broek, R.P.G., Huisman, H.: Medical diffusion on a budget: textual inversion for medical image generation (2023) [arXiv:2303.13430](https://arxiv.org/abs/2303.13430) [cs.CV]
- [33] Akrouf, M., Gyepesi, B., Holló, P., Poór, A., Kincsó, B., Solis, S., Cirone, K., Kawahara, J., Slade, D., Abid, L., Kovács, M., Fazekas, I.: Diffusion-based data augmentation for skin disease classification: Impact across original medical datasets to fully synthetic images (2023) [arXiv:2301.04802](https://arxiv.org/abs/2301.04802) [cs.LG]
- [34] Pernias, P., Rampas, D., Richter, M.L., Pal, C.J., Aubreville, M.: Wuerstchen: An efficient architecture for large-scale text-to-image diffusion models (2023) [arXiv:2306.00637](https://arxiv.org/abs/2306.00637) [cs.CV]
- [35] Ho, J., Salimans, T.: Classifier-free diffusion guidance (2022) [arXiv:2207.12598](https://arxiv.org/abs/2207.12598)

[cs.LG]

- [36] Li, S., Zhao, Y., Varma, R., Salpekar, O., Noordhuis, P., Li, T., Paszke, A., Smith, J., Vaughan, B., Damania, P., Chintala, S.: Pytorch distributed: Experiences on accelerating data parallel training (2020) [arXiv:2006.15704](#) [cs.DC]
- [37] Bar-Tal, O., Chefer, H., Tov, O., Herrmann, C., Paiss, R., Zada, S., Ephrat, A., Hur, J., Liu, G., Raj, A., Li, Y., Rubinstein, M., Michaeli, T., Wang, O., Sun, D., Dekel, T., Mosseri, I.: Lumiere: A space-time diffusion model for video generation (2024) [2401.12945](#) [cs.CV]
- [38] Qing, Z., Zhang, S., Wang, J., Wang, X., Wei, Y., Zhang, Y., Gao, C., Sang, N.: Hierarchical spatio-temporal decoupling for text-to-video generation (2023) [arXiv:2312.04483](#) [cs.CV]
- [39] Oquab, M., Darcet, T., Moutakanni, T., Vo, H., Szafraniec, M., Khalidov, V., Fernandez, P., Haziza, D., Massa, F., El-Nouby, A., Assran, M., Ballas, N., Galuba, W., Howes, R., Huang, P.-Y., Li, S.-W., Misra, I., Rabbat, M., Sharma, V., Synnaeve, G., Xu, H., Jegou, H., Mairal, J., Labatut, P., Joulin, A., Bojanowski, P.: DINOv2: Learning robust visual features without supervision (2023) [2304.07193](#) [cs.CV]
- [40] Heusel, M., Ramsauer, H., Unterthiner, T., Nessler, B., Hochreiter, S.: "gans trained by a two time-scale update rule converge to a local nash equilibrium" (2018) [cs.LG:1706.08500](#) [cs.LG]
- [41] Unterthiner, T., Steenkiste, S., Kurach, K., Marinier, R., Michalski, M., Gelly, S.: Towards accurate generative models of video: A new metric & challenges (2018) [1812.01717](#) [cs.CV]
- [42] Jang, S.-I., Lois, C., Thibault, E., Becker, J.A., Dong, Y., Normandin, M.D., Price, J.C., Johnson, K.A., Fakhri, G.E., Gong, K.: Taupetgen: Text-conditional tau pet image synthesis based on latent diffusion models (2023) [2306.11984](#) [cs.CV]
- [43] Hamamci, I.E., Er, S., Sekuboyina, A., Simsar, E., Tezcan, A., Simsek, A.G., Esirgun, S.N., Almas, F., Dogan, I., Dasdelen, M.F., Prabhakar, C., Reynaud, H., Pati, S., Bluethgen, C., Ozdemir, M.K., Menze, B.: Generatect: Text-conditional generation of 3d chest ct volumes (2024) [arXiv:2305.16037](#) [cs.CV]
- [44] Wang, Z., Bovik, A.C., Sheikh, H.R., Simoncelli, E.P.: Image quality assessment: From error visibility to structural similarity. *IEEE Transactions on Image Processing* **13**(4), 600–612 (2004)